



Ag-AgI/Bi₃O₄Cl for efficient visible light photocatalytic degradation of methyl orange: The surface plasmon resonance effect of Ag and mechanism insight



Boran Xu^{a,b}, Yandong Li^b, Yangqin Gao^b, Shuang Liu^b, Da Lv^b, Sujun Zhao^b, Hang Gao^b, Guoqing Yang^b, Ning Li^b, Lei Ge^{a,b,*}

^a State Key Laboratory of Heavy Oil Processing, College of New Energy and Materials, China University of Petroleum Beijing, No. 18 Fuxue Rd., Beijing 102249, People's Republic of China

^b Department of Materials Science and Engineering, College of New Energy and Materials, China University of Petroleum Beijing, No. 18 Fuxue Rd., Beijing 102249, People's Republic of China

ARTICLE INFO

Keywords:
Photocatalyst
Bi₃O₄Cl
Silver iodine
Surface plasmon resonance
Degradation

ABSTRACT

A novel plasmonic photocatalysts of Ag-AgI/Bi₃O₄Cl was successfully synthesized via a simple and mild wet-chemical process. The 30 wt% Ag-AgI/Bi₃O₄Cl photocatalyst showed the highest photocatalytic activity for degradation of methyl orange (MO) under visible light (5 W LED lamp), which represents a 3.2 and 7.4 times enhancement in the photocatalytic degradation efficiency as compared to pure Bi₃O₄Cl and Ag-AgI, respectively. The surface plasmon resonance (SPR) effect of Ag nanoparticles (NPs) was detected by the UV-vis diffusion reflectance spectroscopy (DRS) and surface photovoltage (SPV) measurement, finding that the SPR effect of Ag extends the absorption and photo-response range in the Ag-AgI/Bi₃O₄Cl composite photocatalyst. Based on the analysis of electron spin resonance (ESR), linear sweeping voltammetry (LSV) characterization results, three electron transfer processes were proposed: AgI_{CB} → Bi₃O₄Cl_{CB}, AgI_{CB} → Ag and methyl orange → Ag. Such electron transfer paths can not only effectively improve the separation efficiency of photo-generated carriers, but also ensure the stability of the catalyst. This study can provide a novel insight for modification of other desirable semiconductor materials to achieve high photocatalytic activity.

1. Introduction

In recent years, how to handle water pollution in a simple way has became a hot research topic with practical concerns. Photocatalytic water treatment utilizing photocatalysts to remove contaminants in air and water with the assistance of solar energy, and therefore has attracted a great attention as an environmentally friendly technology [1–6]. Bismuth-based photocatalysts such as Bi₂WO₆, BiVO₄ and Bi₂Mo₆ are recently recognized as an important class of photocatalysts that fit the requirements for such water treatment application [7–13]. This series of semiconductors have unique layer stacking structure that permits a high separation efficiency of photo-generated carriers. Among them, bismuth oxychlorides have been considered as immense important materials due to their outstanding optical and electrical properties [14,15].

Lots of research focused on BiOCl has been carried out recently. Li's

group explored the synthesis strategies and growth mechanisms of layer-structured bismuth oxyhalide [16]. Xiong and his colleagues found square-like 2D BiOCl nanoplates could exhibit good photocatalytic activity, they attribute the good photocatalytic activity of the BiOCl nanoplates to the synergistic effect of the layer structure, which might allow more efficient transport of the injected electrons [17]. However, the application of BiOCl is highly limited by its low light absorption and large energy loss [18]. In this situation, Bi₃O₄Cl, an alternative photocatalyst that can be excited by visible light, has aroused growing research interest. Huang confirmed that Bi-based oxychloride Bi₃O₄Cl exhibits photocatalytic degradation activity to methyl orange in water under visible-light irradiation [19]. Zhang et al. has prepared single-crystalline Bi₃O₄Cl nanosheets with highly exposed (001) facet, which showed efficient visible-light photocatalytic activity [20]. On the basis of a comprehensive literature study, we notice that Bi₃O₄Cl photocatalyst still exhibits limited photo-catalytic performance

* Corresponding author at: State Key Laboratory of Heavy Oil Processing, College of New Energy and Materials, China University of Petroleum Beijing, No. 18 Fuxue Rd., Beijing 102249, People's Republic of China.

E-mail address: gelei08@sina.com (L. Ge).

under visible light irradiation. Therefore, functional modifications are highly desired for this kind of photocatalyst.

It is well known that Ag nanoparticles (NPs) could absorb visible light arising from their surface plasmon resonance (SPR) [21], but they are easily decomposed under sunlight irradiation. Combing Ag NPs with AgX (Cl, Br and I) to form Ag/AgX composites can efficiently alleviate the decomposing restriction of Ag NPs. Furthermore, the highly dispersed AgX species can improve the separation efficiency of photo-generated charge carriers, and enhance the photocatalytic activity of the supporting photocatalysts [22–24]. Nevertheless, the exact mechanism of this enhanced photo-activity has been rarely studied.

Herein, Ag/AgI modified Bi₃O₄Cl was prepared for the first time using the deposition-precipitation and photo-reduction method, and the effect of loading amount of Ag/AgI on the photocatalytic performance of Bi₃O₄Cl was investigated in detail. Furthermore, the photocatalytic mechanism was verified by electron spin resonance (ESR), surface photovoltage spectroscopy (SPV) and cyclic voltammetry (CV) analysis. According to this study, photo-generated electrons will transfer from AgI to Ag, from AgI to Bi₃O₄Cl and from methyl orange to the silver, and then enhancing the photocatalytic activity and photocatalytic stability of Bi₃O₄Cl in the degradation of methyl orange.

2. Experimental

2.1. Materials

Bismuth nitrate pentahydrate (Bi(NO₃)₃·5H₂O, Aladdin, 98% A.C.S), sodium chloride (NaCl, 99.5% A.R.), sodium iodide (NaI, 99.5% A.R.), ammonia water (NH₃·H₂O, 25%), silver nitrate (AgNO₃, Sigma-Aldrich, 99%) and methyl orange (MO, A.R.) were used as received without additional purification or treatment. Deionized water was used in all experiments.

2.2. Synthesis of the Bi₃O₄Cl nanosheets

In a typical procedure, 3.88 g of Bi(NO₃)₃·5H₂O and 0.234 g of NaCl were added in 48 ml of distilled water at room temperature with continuous stirring, and then 25 wt % ammonia was added to adjust the pH of the solution to 11. The solution was then stirred vigorously for 30 min and transferred into a 100 ml Teflon-lined stainless autoclave, which was heated up to 220 °C for 18 h and air cooled to room temperature. The resulting precipitates were collected, then washed with ethanol and deionized water thoroughly, and finally dried at 50 °C in air. The precipitate was washed by centrifugation, rinsed with distilled water and absolute alcohol, and then dried at 50 °C in air.

2.3. Synthesis of Ag-AgI/Bi₃O₄Cl

0.18 g Bi₃O₄Cl was added to 60 ml distilled water to get solution A, and the suspension was sonicated for 30 min. Then, 0.1 g NaI was added into solution A to form solution B. 0.0145 g AgNO₃ (mass ratio of AgI to AgI/Bi₃O₄Cl was 10%) were added to 20 ml distilled water (named as solution C). Solution C was added drop-wise into solution B with vigorous stirring. The resulting suspension was stirred at room temperature for 30 min. All the above processes were performed in the dark. The products were filtered, washed with distilled water to remove residual ions (Na⁺ and I⁻).

The synthesis process of Ag-AgI/Bi₃O₄Cl composite was described as follows: 0.3 g AgI/Bi₃O₄Cl dispersed into 20 ml deionized water solution. Then, Ag nanoparticles were obtained on the surface of AgI by photo-reduction technique. In the photo-reduction process, the suspension was illuminated by solar simulator 300 W Xe lamp (PLS-SXE300, Beijing Perfect Light Technology Co., Ltd.) for 30 min. All the samples were finally collected after centrifugation washed with ethanol and deionized water; the final products were dried at 50 °C for 12 h and named as 10 wt% Ag-AgI/Bi₃O₄Cl (AAB-10). Similarly, pure Bi₃O₄Cl

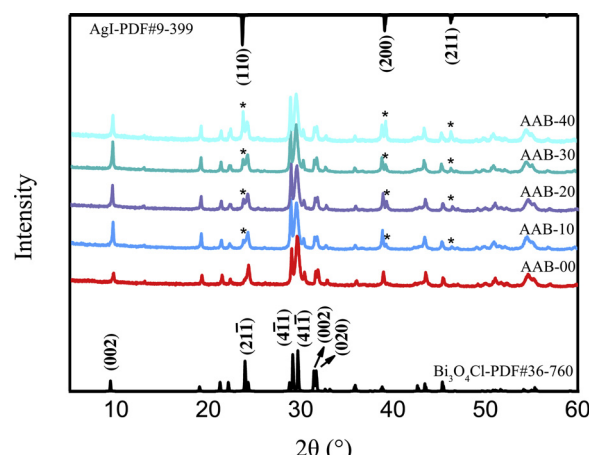


Fig. 1. XRD patterns of AAB-00, AAB-10, AAB-20, AAB-30 and AAB-40.

(AAB-00), 20 wt% Ag-AgI/Bi₃O₄Cl (AAB-20), 30 wt% Ag-AgI/Bi₃O₄Cl (AAB-30), 40 wt% Ag-AgI/Bi₃O₄Cl (AAB-40) and pure Ag/AgI samples were prepared.

2.4. Characterization

The crystal structure of the sample was analyzed by X-ray diffraction with CuK radiation (XRD; Bruker D8 Advance, X-ray diffractometer) at a scanning step of 3°. The morphology of the sample was examined by high-resolution transmission electron microscopy (HRTEM). The X-ray photoelectron spectrometer (XPS) was measured on a PHI 5300 ESCA system with a beam voltage of 3.0 eV and an Ar ion beam energy of 1.0 k eV to detect the composition of the final product. Total organic carbon (TOC) was analyzed by a TOC measuring instrument (Shimadzu TOC-5000). The binding energy was normalized to an indefinite carbon signal at 284.8 eV. Electron spin resonance (ESR) signals of spin-captured oxidized radicals were obtained on a Bruker-type ESR JES-FA200 spectrometer equipped with a quantum ray Nd: YAG laser as a light source, using UV cut-off filter (nm ≥ 400).

2.5. SPV measurements

The surface photovoltage (SPV) measurement was carried out on a surface photovoltage spectroscopy (PL-SPS/IPCE1000 Beijing Perfect Light Technology Co., Ltd.). The measurement system consists of a source of monochromatic light, a lock-in amplifier (SR830, Stanford research systems, Inc.) with a light chopper (SR540, Stanford research systems, Inc.), and a simple chamber. The monochromatic light is provided by passing light from a 500 W xenon lamp (CHFXQ500 W, global xenon lamp power) through a grating monochromator (Omni-5007, No. 09010, Zolix), which chopped with a frequency of 24 Hz. All the measurements were operated at room temperature and under ambient pressure.

2.6. Electrochemical characterization

All electrochemical characterizations were performed on a CHI 760e electrochemical workstation using 0.1 M sodium sulfate solution as the electrolyte. A three electrode setup was used to perform linear sweeping voltammetry (LSV) measurements where tested sample, Pt wire and Hg/Hg₂Cl₂ (3 M KCl) electrode worked as working electrode, counter electrode and reference electrode, respectively. LSV was measured at a scan rate of 5 mV s⁻¹ unless otherwise noted. The bias potential was referenced to reverse hydrogen electrode (RHE) by the Nernst equation, where VRHE = V_{Hg/Hg₂Cl₂} + 0.0592 V × pH + 0.244 V. Electrochemical impedance spectroscopy (EIS) was performed on a CHI 760e electrochemical workstation with an AC amplitude of 10 mV and

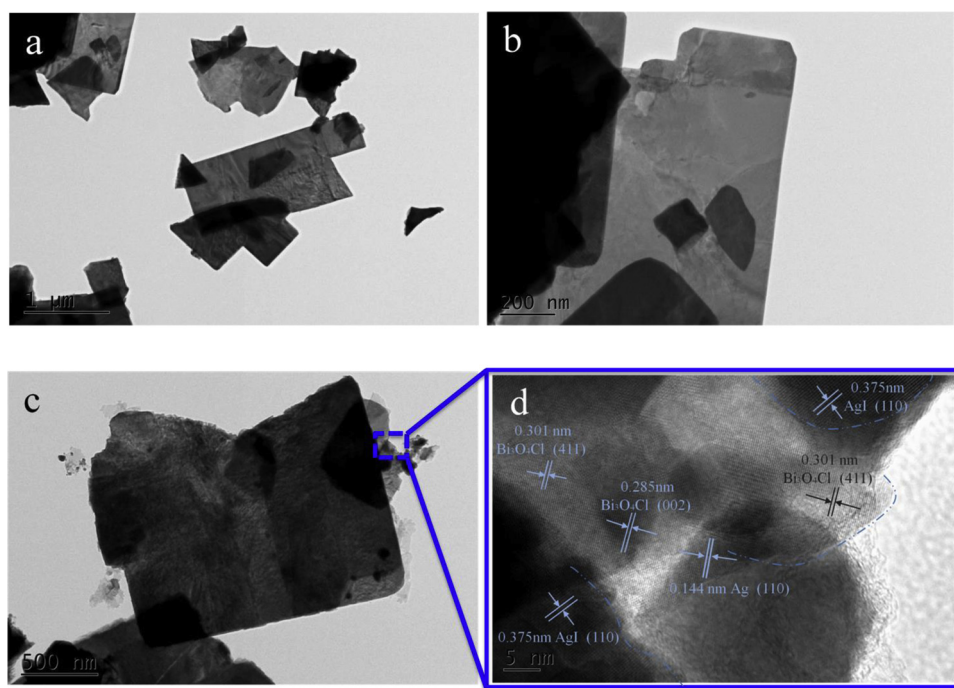


Fig. 2. (a),(b) TEM image of $\text{Bi}_3\text{O}_4\text{Cl}$ (c) TEM image of $\text{Ag}-\text{AgI}/\text{Bi}_3\text{O}_4\text{Cl}$ and (d) HRTEM image of $\text{Ag}-\text{AgI}/\text{Bi}_3\text{O}_4\text{Cl}$ nanosheets.

frequency range between 100 KHz to 0.1 Hz. The measured EIS data were obtained at an applied bias of 0 V vs. $\text{Hg}/\text{Hg}_2\text{Cl}_2$ at 25 °C.

2.7. Photocatalytic activity

The photocatalytic activities of the as-prepared samples were investigated by degradation of MO under visible-light irradiation using the Discover- Multichannel photocatalytic reaction system (PCX50 A Beijing Perfect Light Technology Co., Ltd.). 10 mg photocatalyst powder was suspended in 50 ml MO aqueous solution (20 mg/l). The suspension was stirred for 30 min in the dark to establish adsorption-desorption equilibrium. After that, one 5 W LED lamp (white-light source) was used as the visible light source to irradiate the suspensions under vigorous stirring. The light intensity employed was 80 $\text{mW}\cdot\text{cm}^{-2}$. After irradiation, 1 ml sample solution was collected at certain time interval, the photocatalysts were removed by centrifugation, and the remaining solution was analyzed on the UV-vis spectrometer.

3. Results and discussion

3.1. Characterization of the $\text{Ag}-\text{AgI}/\text{Bi}_3\text{O}_4\text{Cl}$ nanosheets

The composition and phase structure of the sample were investigated by XRD, which were shown in Fig. 1. All of the peaks in the XRD pattern of AAB-00 could be indexed to $\text{Bi}_3\text{O}_4\text{Cl}$ (JCPDS File No. 37-760). The main peaks at 2θ of 9.50°, 23.98°, 29.12°, 29.68°, 31.40° and 31.66° can be readily indexed to the (200), (21), (41), (41), (002) and (020) planes of $\text{Bi}_3\text{O}_4\text{Cl}$. And the diffraction peaks appearing at 2θ of 24.86°, 35.46°, and 43.78° after loading of AgI can be assigned to the (110), (200) and (211) planes of AgI (JCPDS File No. 20-1058). It is obvious that the diffraction intensity of the AgI peaks is enhanced gradually with increasing the loading ratio of AgI. By comparing the diffraction pattern of $\text{Bi}_3\text{O}_4\text{Cl}$ and AgI modified $\text{Bi}_3\text{O}_4\text{Cl}$, it can be concluded that the deposition process of AgI did not affect the crystal structure of $\text{Bi}_3\text{O}_4\text{Cl}$. However, no characteristic peak of Ag is detected, implying a very low content of Ag or a high dispersion of Ag in the composites. No characteristic peaks attributing to impurities or other phases can be detected.

To confirm the successful loading of Ag on the surface of $\text{Bi}_3\text{O}_4\text{Cl}$, the $\text{Ag}-\text{AgI}/\text{Bi}_3\text{O}_4\text{Cl}$ sample was further investigated by TEM and HRTEM (Fig. 2). It can be seen that the $\text{Bi}_3\text{O}_4\text{Cl}$ sample is composed by layer-stacked nanosheets. In the $\text{Ag}-\text{AgI}/\text{Bi}_3\text{O}_4\text{Cl}$ sample, Ag/AgI was deposited as nanoparticles on the surface of $\text{Bi}_3\text{O}_4\text{Cl}$ with high dispersion. Except of the deposition of Ag/AgI, no other obvious changes in the microstructure of $\text{Bi}_3\text{O}_4\text{Cl}$ nanosheets can be found. The HRTEM images in Fig. 2c and d present several lattice fringes with the spacing of 0.250, 0.301, 0.144 and 0.375 nm, which can be indexed to the (121), (411) plane of $\text{Bi}_3\text{O}_4\text{Cl}$, (110) plane of AgI, and (110) plane of Ag, respectively. The arrangement of Ag, AgI with $\text{Bi}_3\text{O}_4\text{Cl}$ can be clearly recognized from HRTEM, that is, AgI adheres to the surface of $\text{Bi}_3\text{O}_4\text{Cl}$ with Ag nanoparticles distributing around. This result further confirms that the surface of the $\text{Bi}_3\text{O}_4\text{Cl}$ nanosheets are decorated by the Ag-AgI nanoparticles.

The chemical states of each element in the AAB-30 sample were further explored by X-ray photoelectron spectroscopy (XPS), proved the sample is only composed by five elements, which are Bi, O, Cl, Ag and I (Fig. 3f). Fig. 3a presents Ag 3d XPS spectrum of $\text{Ag}-\text{AgI}/\text{Bi}_3\text{O}_4\text{Cl}$. The peaks observed at 367.3 and 373.3 eV can be ascribed to binding energies of Ag 3d5/2 and Ag 3d3/2, respectively [22,25]. And two small peaks at 368.3 and 373.9 eV were assigned to Ag° species [22,26]. The results indicate that Ag element exists both in the form of Ag^+ and Ag° . In Fig. 3b, the peaks at 619.51 and 631.02 eV corresponding to I 3f_{3/2} and I 3f_{5/2} are related to I⁻ in AgI [25,27]. Fig. 3c illustrates the binding energies of Bi 4f at 159.14 and 164.47 eV, which are assigned to Bi 4f_{7/2} and Bi 4f_{5/2}, respectively [28,29]. Fig. 3d gives the binding energies of O 1s in the samples, of 530.01 eV and 531.49 eV [10], respectively. In Fig. 3e, the peaks at 198.07 eV and 199.65 eV are assigned to Cl 2f_{1/2} and Cl 2f_{3/2}, respectively [18]. In addition, the valence band (VB) of $\text{Bi}_3\text{O}_4\text{Cl}$ was investigated by XPS valence spectra (Fig. 4) [12,25]. And the VB maximum of $\text{Bi}_3\text{O}_4\text{Cl}$ is estimated to be 3.2 eV, which can be used to figure out the band structure of $\text{Bi}_3\text{O}_4\text{Cl}$ as discussed later.

3.2. Visible light photocatalytic activity of $\text{Ag}-\text{AgI}/\text{Bi}_3\text{O}_4\text{Cl}$ nanosheets

After the adsorption of MO onto the surface of photocatalysts in

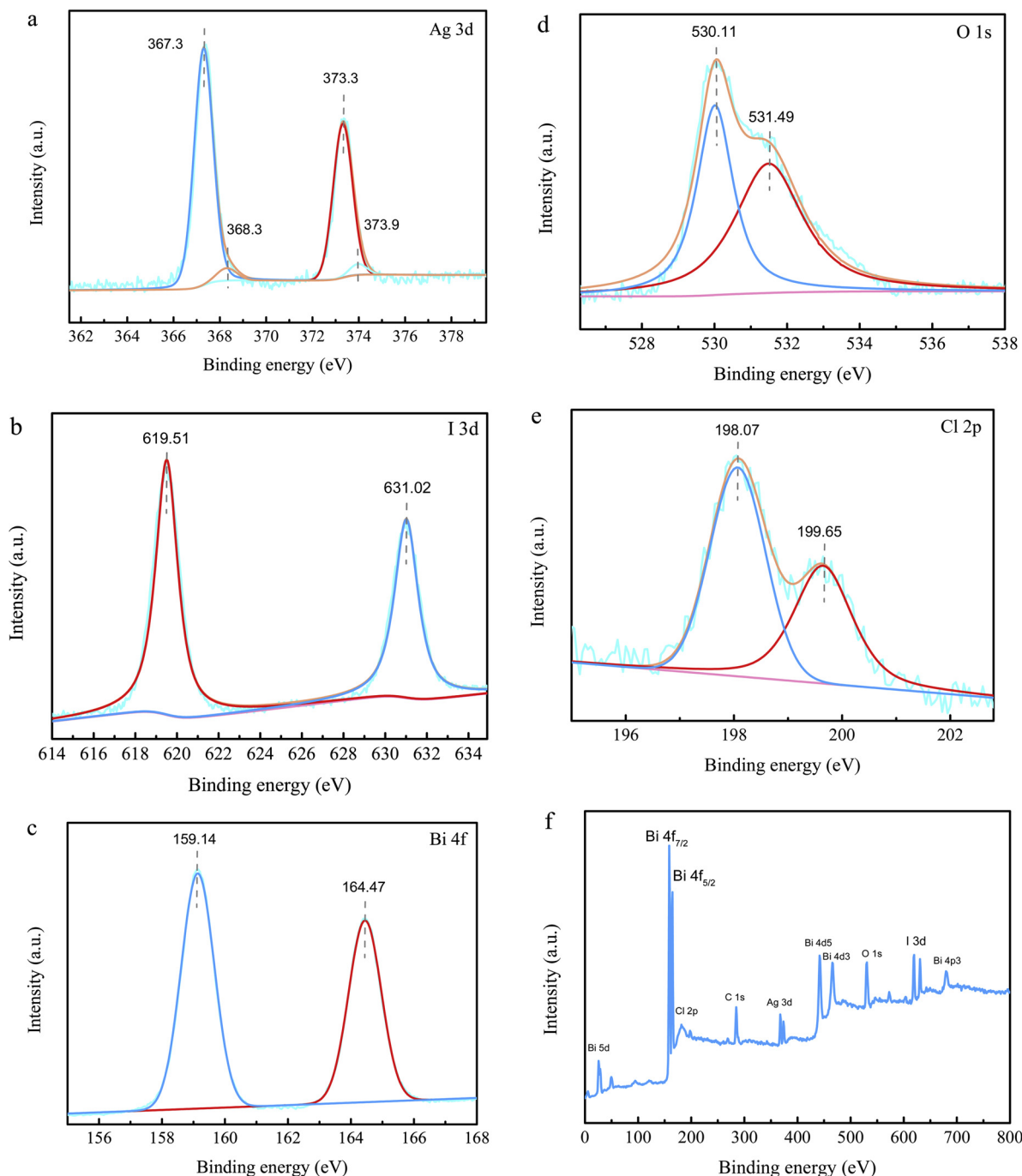


Fig. 3. XPS spectra of Ag-AgI/Bi₃O₄Cl sample: (a) Ag 3d (b) I 3f (c) Bi 4f; (d) O 1 s; (e) Cl 2p; (f) survey.

dark to reach equilibrium, photo degradation of MO was carried out under visible light irradiation to evaluate the photocatalytic activities of the as-prepared samples (Fig. 5a). The pure Bi₃O₄Cl sample without Ag-AgI deposition exhibits low photo degradation activity, only 19% MO was decomposed after 180 min. After surface deposition of Ag-AgI, all of the Ag-AgI/Bi₃O₄Cl composite samples exhibit significantly enhanced photocatalytic activity. The photocatalytic performance of the Ag-AgI/Bi₃O₄Cl composite sample was reached highest as the loading ratio of Ag-Ag is at 30 wt%. Here, it should be noted that Ag-AgI alone showed a even poorer photocatalytic performance as compared to pure Bi₃O₄Cl. The effect of Ag weight fraction on the photocatalytic performance of the composite sample was also investigated, the weight fraction of Ag was adjusted by controlling the photo-reduction duration when preparing the 30 wt% Ag-AgI/Bi₃O₄Cl sample (Fig. 5c). In the

absence of photo-reduction 30 wt% AgI/Bi₃O₄Cl without formation of Ag NPs was expected, and only 32% of MO was degraded. Along with increasing the photo-reduction duration, that is increasing the weight fraction of Ag in the composites, the photocatalytic degradation rate of MO was improved. And when the photo-reduction time was reached to 60 min, the photocatalytic degradation of MO was remarkably increased to 61% after 180 min visible light irradiation. To give a quantitative investigation on the reaction kinetics of the photo-degradation process of MO, the photo-degradation results were fitted by applying a first-order model (Fig. 5b and d). It can be seen that ln (C₀/C) and irradiation duration can be fitted into a linear law, which gives a preliminary proof of the stability of the photocatalyst [30]. The degradation rate constant of 30 wt% Ag-AgI/Bi₃O₄Cl with photo-reduction duration of 60 min was improved for about 3.2 and 7.4 times as

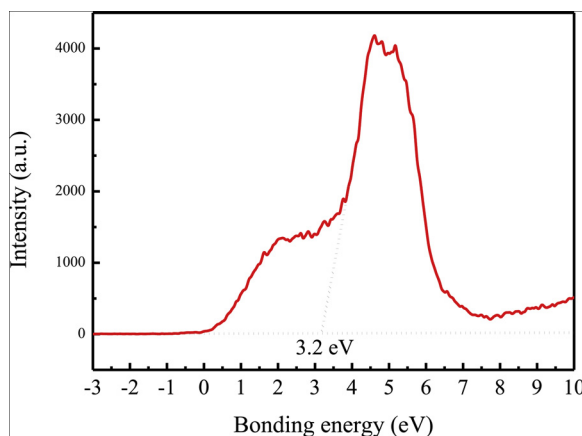


Fig. 4. Valence band XPS spectra of $\text{Bi}_3\text{O}_4\text{Cl}$.

compared to that of pure $\text{Bi}_3\text{O}_4\text{Cl}$ and Ag-AgI, respectively.

To further verify the successful degradation of MO, the total organic carbon (TOC) of the solution was analyzed. Fig. 6 shows the TOC removal of MO vs irradiation time for the sample of 30 wt% Ag-AgI/ $\text{Bi}_3\text{O}_4\text{Cl}$ nanosheets. It can be seen that the mineralization degree of MO reached 48% after visible light irradiation of 3 h, which was a little bit lower comparing with the bleaching ratio of the MO solution. This mismatch between TOC and UV-vis characterization indicates that a certain ratio of MO converts into colorless compound instead of being

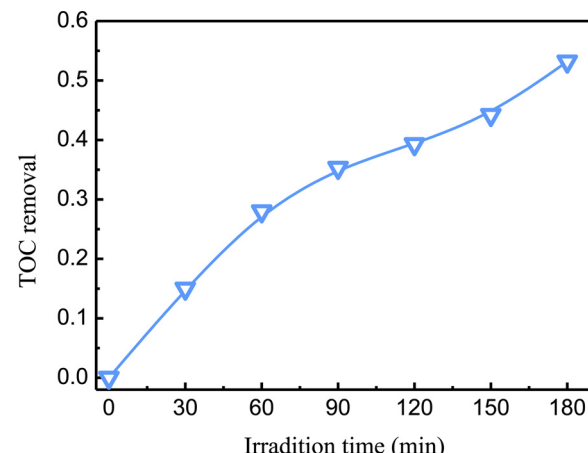


Fig. 6. TOC removal of MO vs irradiation time for the sample of 30 wt% Ag-AgI/ $\text{Bi}_3\text{O}_4\text{Cl}$.

fully derogated into volatile products.

Since the practical application of photocatalysts calls for good stability, cycle runs of photo-oxidation of MO were performed using the 30 wt% Ag-AgI/ $\text{Bi}_3\text{O}_4\text{Cl}$ nanosheets to show the stability. Fig. 7 presents that the photocatalyst still maintain its photocatalytic degradation activity of MO after four cycle runs, indicating a reliable photocatalytic stability.

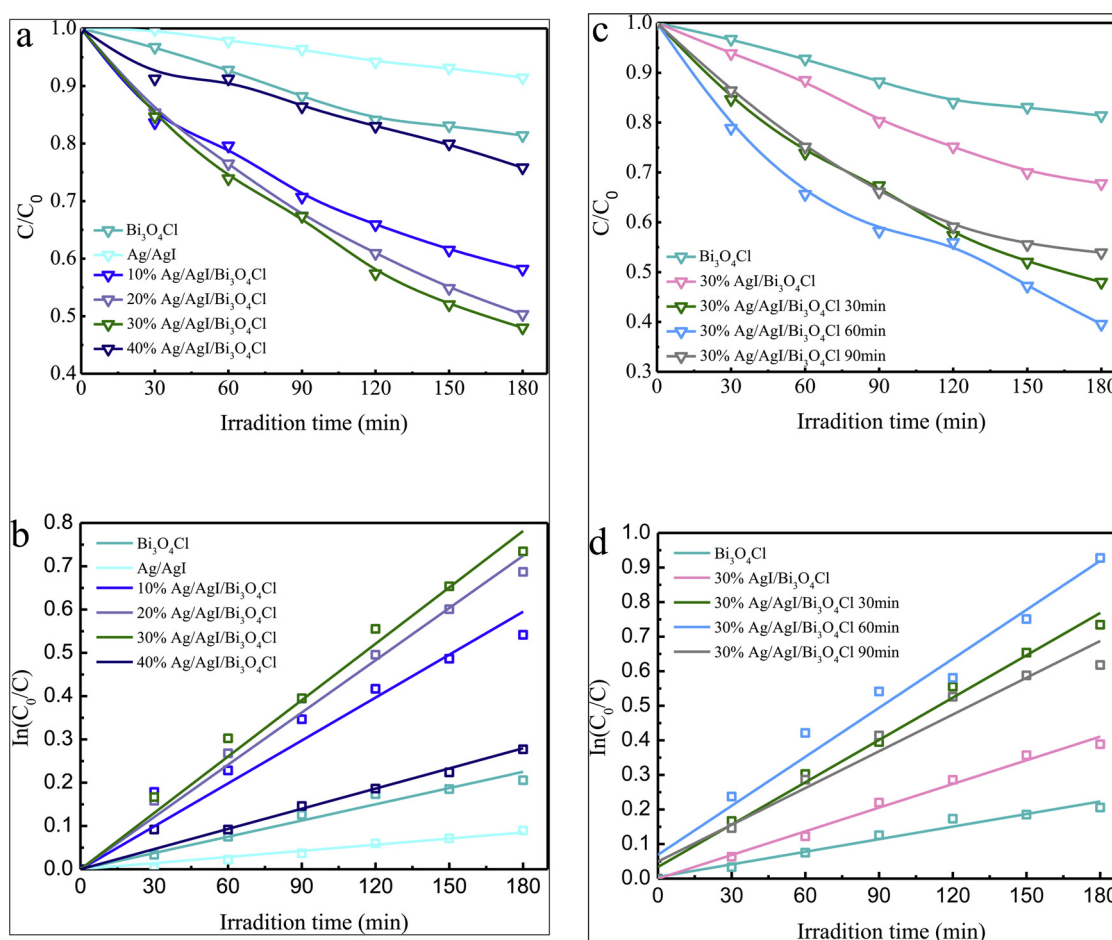


Fig. 5. (a) Dependence of photocatalytic activity on the weight ratios of Ag-AgI. (b) Relationship between $\ln(\text{C}_0/\text{C})$ and irradiation time of different weight ratios of Ag-AgI (c). Dependence of photocatalytic activity on the photoreduction time of Ag (d). Relationship between $\ln(\text{C}_0/\text{C})$ and irradiation time of different photoreduction time.

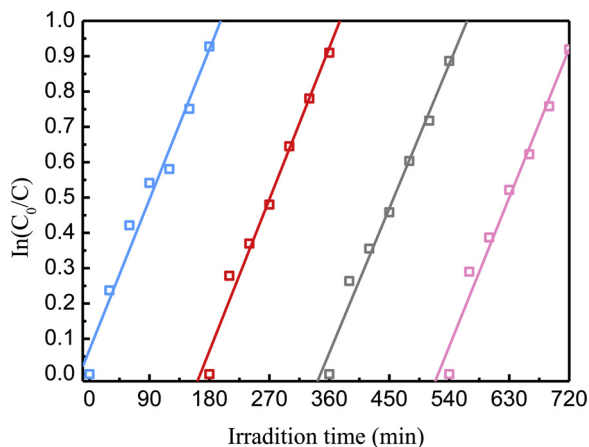


Fig. 7. Cycling runs for the photocatalytic degradation of methyl orange in the presence of 30 wt% Ag-AgI/Bi₂₄O₃₁Cl₁₀ composite under visible light irradiation.

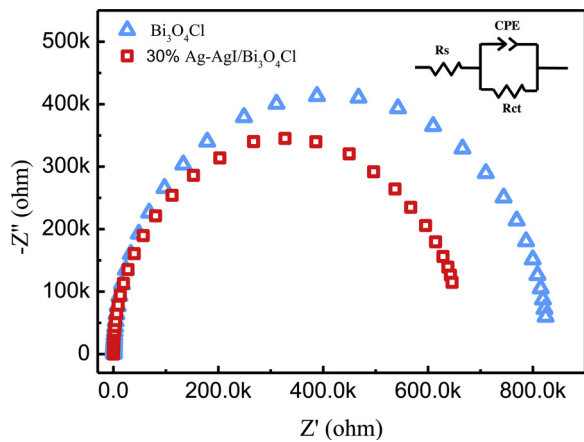


Fig. 8. EIS spectra of Bi₃O₄Cl and Ag-AgI/Bi₃O₄Cl.

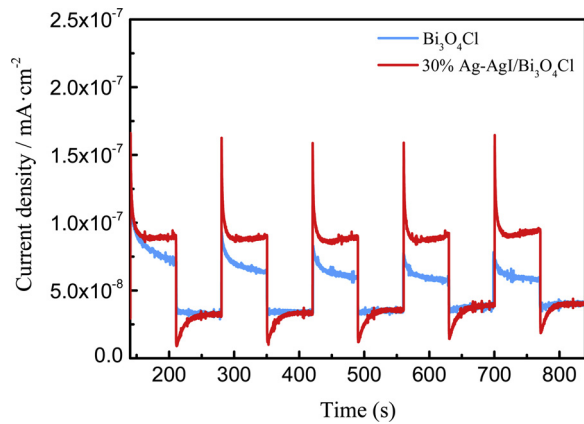


Fig. 9. Transient photocurrent of Bi₃O₄Cl and Ag-AgI/Bi₃O₄Cl.

3.3. Photocatalytic mechanism discussion

To explore the photocatalytic activity enhancement mechanism of Ag-AgI/Bi₃O₄Cl, electrochemical impedance spectroscopy (EIS) and transient photocurrent measurements were carried out. The arc radius in EIS spectroscopy represents the surface charge transfer resistance in the redox reaction. A smaller radius in the EIS Nyquist plot indicates a lower impedance and a higher efficiency of charge transfer [31]. As shown in Fig. 8, the radius of the Nyquist plot of AAB-30 is significantly

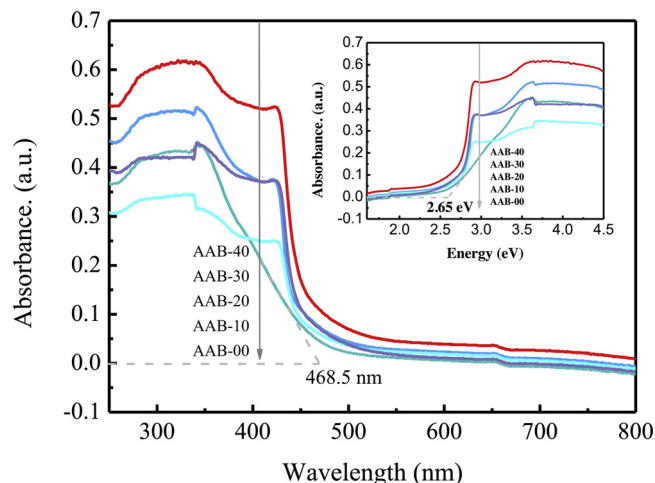


Fig. 10. UV-vis diffuse reflectance spectra of pure Bi₃O₄Cl nanosheets and Ag-AgI/Bi₃O₄Cl composites with different weight ratios of Pt NPs.

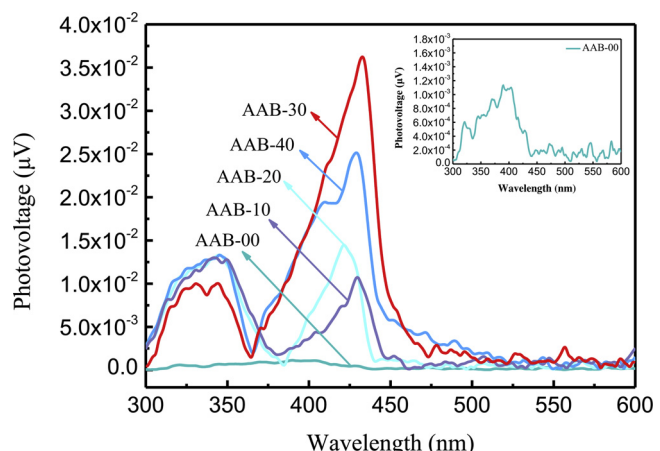


Fig. 11. Surface photovoltage spectra of pure Bi₃O₄Cl nanosheets and Ag-AgI/Bi₃O₄Cl composites with different weight ratios of Pt NPs.

decreased in comparison with Bi₃O₄Cl. These results can be further supported by transient photocurrent measurements as shown in Fig. 9. After loading 30 wt% Ag-AgI on Bi₃O₄Cl, the transient photocurrent density was largely increased, which indicates that the separation efficiency of photo-generated charge carriers is significantly improved, thus extending the lifetime of the electron-hole pairs effectively [32]. When the light is turned off, the dark current is very low and maintains its stable state. It should be noted that the AAB-30 sample shows a quite stable steady state photocurrent at each switching cycle of the light. In contrast, a quick decay in the steady state photocurrent is observed in the pure Bi₃O₄Cl sample. It is worth noting that the photocurrent response of AAB-30 shows a characteristic decay from a “spike” to a steady state upon turning the light on, and a similar cathodic “spike” can also be observed upon turning the light off. This may mean that the surface loaded Ag-AgI can serve as charge storage mediator for the photo-generated carriers in Bi₃O₄Cl [33].

The optical absorption of pure Bi₃O₄Cl and various loading ratios of Ag-AgI in the Ag-AgI/Bi₃O₄Cl nanosheets were characterized by UV-vis spectrometer (Fig. 10). The absorption edge of Bi₃O₄Cl is estimated to be 468.5 nm. And the optical band gap of Bi₃O₄Cl is derived to be 2.65 eV (Fig. 10 inset) according to Tauc formula [34,35]. With increasing the loading amount of Ag-AgI, the absorption intensity in 350–450 nm regions is significantly improved, which can be assigned to the surface plasmon absorption of Ag NPs [36]. Hence the enhanced light absorption arising from the SPR effect is expected to lead to an

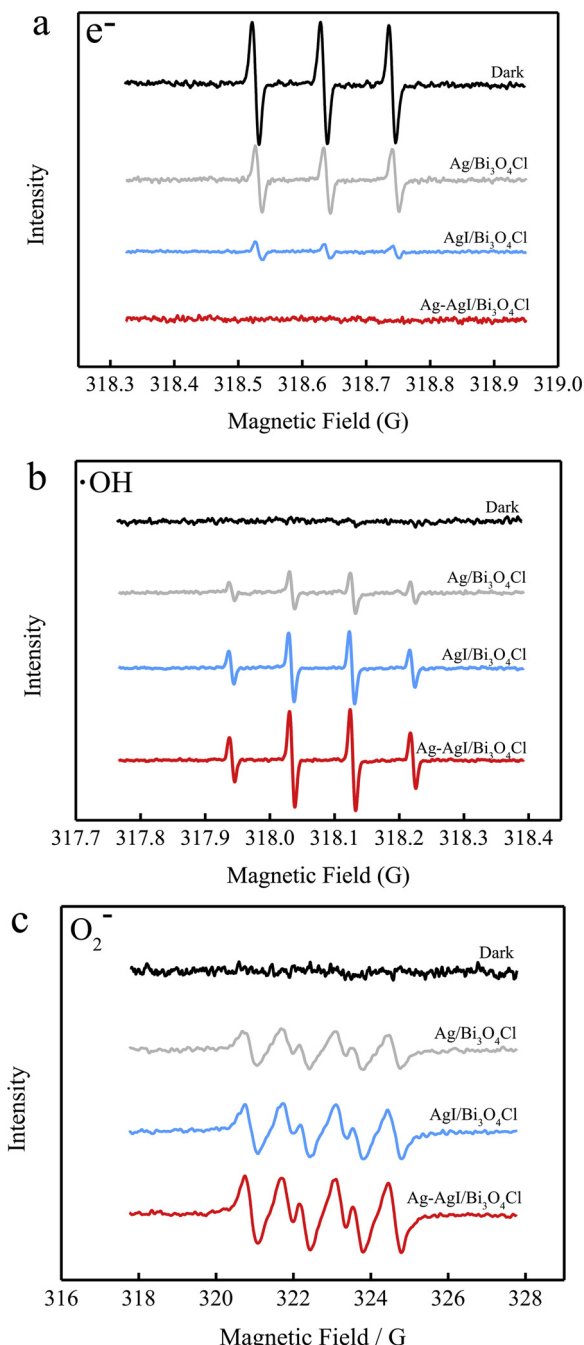


Fig. 12. ESR spectra record of (a) e^- (b) $\cdot OH$ and (c) $\cdot O_2^-$ at ambient temperature with Ag/Bi_3O_4Cl , AgI/Bi_3O_4Cl and $Ag\text{-}AgI/Bi_3O_4Cl$ photo-catalyst.

improved photocatalytic degradation performance.

To further explore the effect of Ag on the photo-generated charge carriers in the composite samples, the surface photovoltage (SPV) technique is employed to investigate the photo-generated charge-transfer properties of $Ag\text{-}AgI/Bi_3O_4Cl$. As is well known, a stronger photoelectric signal corresponds to higher charge separation efficiency [37]. The result shown in Fig. 11 indicates that the separation efficiency of charge carriers in the composite samples is much higher than that in pure Bi_3O_4Cl . And the sample with Ag -loading content of 30 wt% gives the highest SPV response, which is consistent with the photocatalytic degradation result. Fig. 11 inset gives the SPV spectra of Bi_3O_4Cl , which only shows a weak response at the wavelength region from 310 nm to 430 nm. Interestingly, all the composite samples have a strong response at the wavelength region in 420–450 nm that cannot be

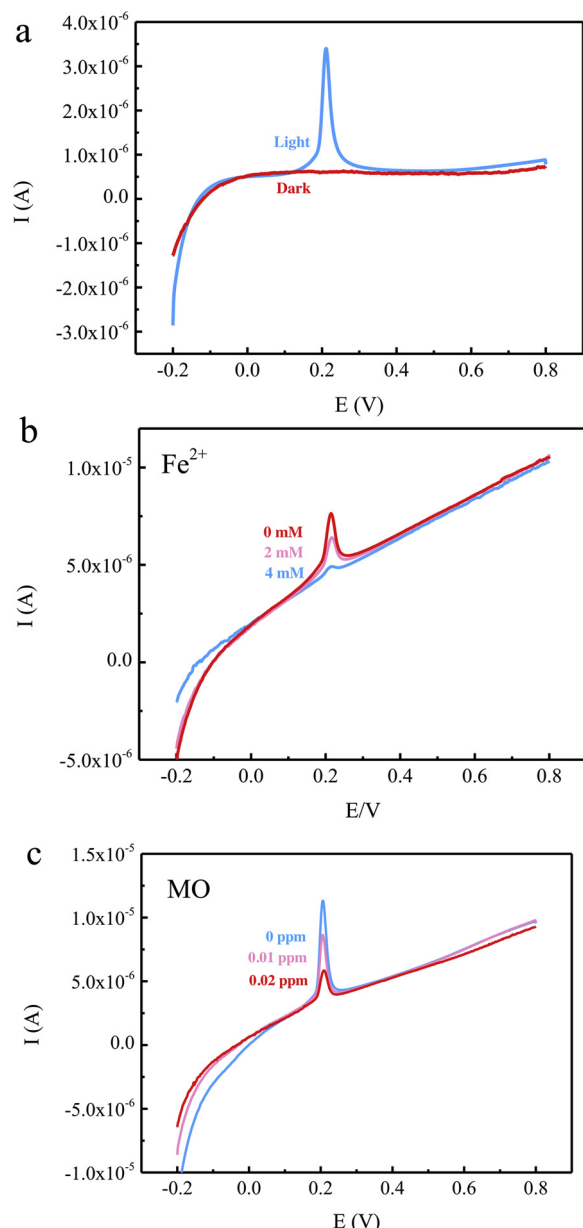
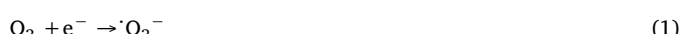


Fig. 13. C-V curves of $Ag\text{-}AgI/Bi_3O_4Cl$ in N_2 -saturated 0.1 M sodium sulfate aqueous solutions under the specified conditions.

detected in pure Bi_3O_4Cl . Combined with the results of DRS analysis, it is safe to say that the SPR effect of Ag can not only extend the absorption range of light, but also improve the photo response of the photocatalyst in the extended light absorption range [36].

Electron spin resonance (ESR) was adopted to explore the active groups in the degradation process. TEMP is the radical scavenger of e^- and is commonly used to detect the number of free electrons in ESR. When $Ag\text{-}AgI/Bi_3O_4Cl$ is exposed under light irradiation, no signal of TEMP was revealed (Fig. 12a), which means light irradiation results in a large amount of electrons that convert TEMP into TEMPO. However, the signal of TEMP can still be clearly detected in Ag/Bi_3O_4Cl and AgI/Bi_3O_4Cl , indicating the low quantity of photo-generated electrons.

It has been proposed that photo-generated electrons usually participate in a two-electron reduction process with the assistance of active molecular oxygen (Eqs. (1) and (2)) [38].



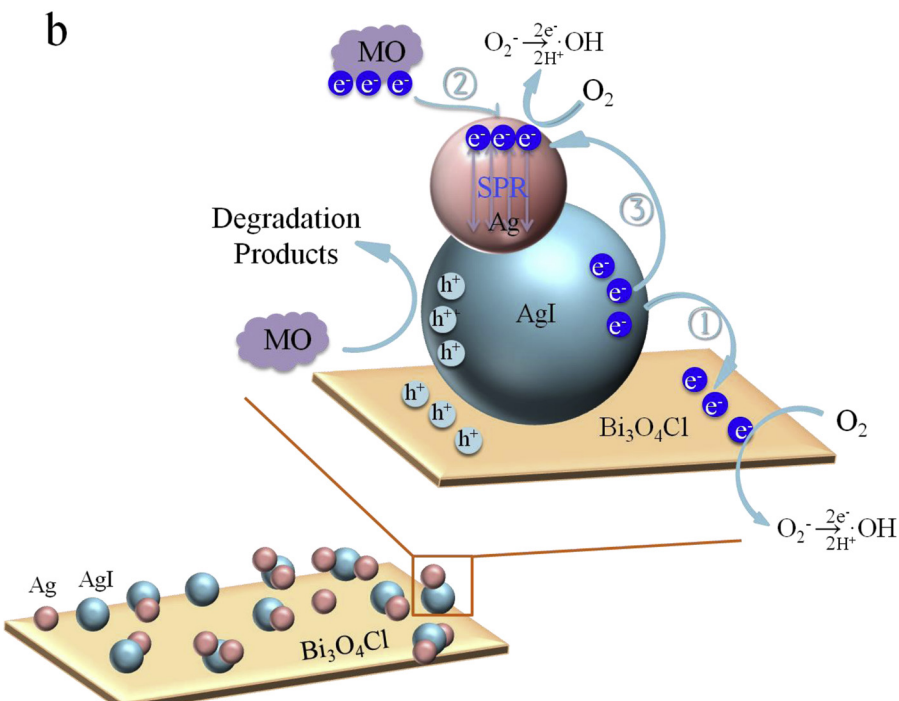
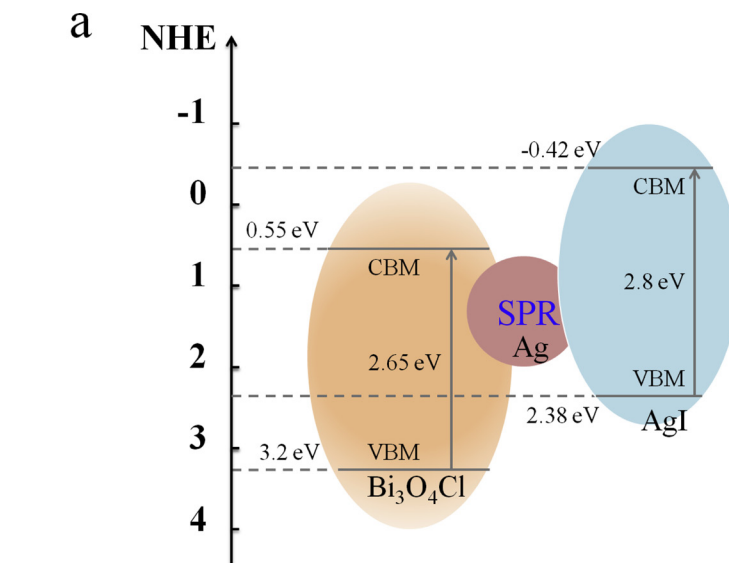


Fig. 14. (a) Band structure (b) Proposed mechanism for photo-catalytic degradation of MO under visible light irradiation.

Therefore the signal of $\cdot\text{OH}$ and $\cdot\text{O}_2^-$ were checked in $\text{Ag-AgI}/\text{Bi}_3\text{O}_4\text{Cl}$, $\text{Ag}/\text{Bi}_3\text{O}_4\text{Cl}$ and $\text{AgI}/\text{Bi}_3\text{O}_4\text{Cl}$ by ESR (Fig. 12b, c) to verify the transfer route of photo-generated electrons. Similarly, no signal of $\cdot\text{OH}$ and $\cdot\text{O}_2^-$ can be seen under dark condition, but both of their ESR peaks can be observed in $\text{Ag-AgI}/\text{Bi}_3\text{O}_4\text{Cl}$ under illuminated conditions, while relatively weak $\cdot\text{OH}$ and $\cdot\text{O}_2^-$ ESR peaks in $\text{Ag}/\text{Bi}_3\text{O}_4\text{Cl}$ and $\text{AgI}/\text{Bi}_3\text{O}_4\text{Cl}$ were observed. The results suggest that e^- , $\cdot\text{OH}$, and $\cdot\text{O}_2^-$ are all main active species involved in the photo-degradation process with the interaction between Ag and AgI.

Furthermore, the transfer approaches of charge carriers were studied by linear sweeping voltammetry (LSV) analysis. In order to eliminate the interference of oxygen in the air, the following tests were carried out in a nitrogen-saturated sodium sulfate solution. As shown in

Fig. 13a, no significant photocurrent was detected in the dark. However, an anodic peak was appeared in the LSV curve under visible irradiation, which was contributed to the oxidation of Ag NPs [39]. Comparing these two different results, it can be easily concluded that the oxidation of Ag NPs is caused by photo-generated h^+ . With the addition of Fe^{2+} ions to act as electron donors, the intensity of the anodic peak starts to decrease and became inconspicuous when the concentration of Fe^{2+} reached 4 mM (Fig. 13b). This result indicated that the photocurrent generation was ascribed to oxidation of Ag under visible light, which could then be reduced by Fe^{2+} . A similar phenomenon was observed after adding methyl orange (Fig. 13c). This means that methyl orange plays the same role as Fe^{2+} to obtain photo stable Ag NPs and stable photocurrent. Based on all of the information,

it can be concluded that photo-generated electrons are very important for the photodegradation of MO. On the other hand, the degradation of MO can also effectively ensure the stability of the photocatalyst.

The main electronic transfer path was inferred based on the band structures of $\text{Bi}_3\text{O}_4\text{Cl}$ and AgI as shown in Fig. 14. The valence band (VB) and energy gap of $\text{Bi}_3\text{O}_4\text{Cl}$ were obtained from the XPS and DRS characterizations. So the top of VB and the bottom of CB of $\text{Bi}_3\text{O}_4\text{Cl}$ were calculated to be 3.2 eV and 0.55 eV, respectively. And the CB of AgI is -0.42 eV [25,27], which means that e^- can easily transfer from AgI to $\text{Bi}_3\text{O}_4\text{Cl}$ (electron transfer 1: $\text{AgI}_{\text{CB}} \rightarrow \text{Bi}_3\text{O}_4\text{Cl}_{\text{CB}}$). The other electron transfer path was from MO to Ag NPs (electron transfer 2: MO \rightarrow Ag) according to the result of LSV. Then Ag NPs were not corrupted by light and resulted in significantly more stable Ag halides. Additionally, because the VB potential of AgI was more positive than the Fermi level of Ag NPs [40], the e^- on the CB of AgI can also easily flow to into the Ag NPs (electron transfer 3: $\text{AgI}_{\text{CB}} \rightarrow \text{Ag}$). Thus, the simultaneous electron transfers would enhance the separation of electron–hole pairs (Fig. 14b) to obtain a better performance photocatalyst after the modification of Ag-AgI.

4. Conclusions

In summary, Ag-AgI/ $\text{Bi}_3\text{O}_4\text{Cl}$ nanosheets were successfully synthesized and exhibited an enhanced photocatalytic performance with improved photocatalytic stability compared with pure $\text{Bi}_3\text{O}_4\text{Cl}$. The DSR and SPV investigations indicate the surface plasmon resonance effect of Ag NPs contributes to the enhanced photocatalytic performance of the Ag-AgI/ $\text{Bi}_3\text{O}_4\text{Cl}$ nanosheets. Three kinds of main active species involved in the photocatalytic degradation process were revealed by ESR. And three electron transfer processes were proposed based on the LSV analysis. This finding indicates that the synergistic effect between the metal nanoparticles with surface plasmon resonance effect and their halide could be applied to modify oxygen-enriched bismuth oxyhalides semiconductor to achieve improved photocatalytic performance.

Acknowledgements

This work was financially supported by the National Science Foundation of China (Grant No. 51572295, 21273285 and 21003157), Beijing Nova Program (Grant No. 2008B76), and Science Foundation of China University of Petroleum, Beijing (Grant No. KYJJ2012-06-20 and 2462016YXBS05).

References

- [1] Z.G. Zou, J.H. Ye, K. Sayama, H. Arakawa, *Nature* 414 (2001) 625–627.
- [2] M.L. Marin, L. Santos-Juanes, A. Arques, A.M. Amat, M.A. Miranda, *Chem. Rev.* 112 (2012) 1710–1750.
- [3] C.C. Chen, W.H. Ma, J.C. Zhao, *Chem. Soc. Rev.* 39 (2010) 4206–4219.
- [4] G. Liu, Y. Zhao, C. Sun, F. Li, G.Q. Lu, H.M. Cheng, *Angew. Chem. Int. Ed.* 47 (2008) 5277–5277.
- [5] M.X. Ji, Y.L. Liu, J. Di, R. Chen, Z.G. Chen, J.X. Xia, H.M. Li, *Appl. Catal. B Environ.* 237 (2018) 1033–1043.
- [6] J. Li, J. Wang, G.K. Zhang, Y. Li, K. Wang, *Appl. Catal. B Environ.* 234 (2018) 167–177.
- [7] P.Z. Cui, J.L. Wang, Z.M. Wang, J. Chen, X.R. Xing, L.Z. Wang, R.B. Yu, *Nano Res.* 9 (2016) 593–601.
- [8] K.F. Zhang, Y.X. Liu, J.G. Deng, S.H. Xie, X.T. Zhao, J. Yang, Z. Han, H.X. Dai, *Appl. Catal. B Environ.* 224 (2018) 350–359.
- [9] G.Y. Long, J.F. Ding, L.H. Xie, R.Z. Sun, M.X. Chen, Y.F. Zhou, X.Y. Huang, G.R. Han, Y.J. Li, W.R. Zhao, *Appl. Surf. Sci.* 455 (2018) 1010–1018.
- [10] J.L. Zhang, Y. Lu, L. Ge, C.C. Han, Y.J. Li, Y.Q. Gao, S.S. Li, H. Xu, *Appl. Catal. B Environ.* 204 (2017) 385–393.
- [11] Y. Bai, X. Shi, P.Q. Wang, H.Q. Xie, L.Q. Ye, *ACS Appl. Mater. Interfaces* 9 (2017) 30273–30277.
- [12] W. Zhao, C. Li, A.J. Wang, C.C. Lv, W.H. Zhu, S.P. Dou, Q. Wang, Q. Zhong, *Phys. Chem. Chem. Phys.* 19 (2017) 28696–28709.
- [13] J. Di, C. Chen, C. Zhu, M.X. Ji, J.X. Xia, C. Yan, W. Hao, S.Z. Li, H.M. Li, Z. Liu, *Appl. Catal. B Environ.* 238 (2018) 119–125.
- [14] J.X. Xia, J. Zhang, S. Yin, H.M. Li, H. Xu, L. Xu, Q. Zhang, *J. Phys. Chem. Solids* 74 (2013) 298–304.
- [15] X. Zhang, Z.H. Ai, F.L. Jia, L.Z. Zhang, *J. Phys. Chem. C* 112 (2008) 747–753.
- [16] J. Li, Y. Yu, L.Z. Zhang, *Nanoscale* 6 (2014) 8473–8488.
- [17] J.Y. Xiong, G. Cheng, G.F. Li, F. Qin, R. Chen, *RSC Adv.* 1 (2011) 1542–1553.
- [18] S.B. Ning, L.Y. Ding, Z.G. Lin, Q.Y. Lin, H.L. Zhang, H.X. Lin, J.L. Long, X.X. Wang, *Appl. Catal. B-Environ.* 185 (2016) 203–212.
- [19] X.P. Lin, T. Huang, F.Q. Huang, W.D. Wang, J.L. Shi, *J. Phys. Chem. B* 110 (2006) 24629–24634.
- [20] J. Li, L.Z. Zhang, J. Li, Y. Yu, *Nanoscale* 6 (2014) 167–171.
- [21] L. Ge, C.C. Han, J. Liu, Y.F. Li, *Appl. Catal. A-Gen.* 409 (2011) 215–222.
- [22] X.X. Li, S.M. Fang, L. Ge, C.C. Han, P. Qiu, W.L. Liu, *Appl. Catal. B-Environ.* 176 (2015) 62–69.
- [23] Z. Wan, G.K. Zhang, *J. Mater. Chem. A* 3 (2015) 16737–16745.
- [24] D.D. Tang, J. Li, G.K. Zhang, *Appl. Catal. B-Environ.* 224 (2018) 433–441.
- [25] S.B. Ning, H.X. Lin, Y.C. Tong, X.Y. Zhang, Q.Y. Lin, Y.Q. Zhang, J.L. Long, X.X. Wang, *Appl. Catal. B-Environ.* 204 (2017) 1–10.
- [26] L.Q. Ye, J.Y. Liu, C.Q. Gong, L.H. Tian, T.Y. Peng, L. Zan, *ACS Catal.* 2 (2012) 1677–1683.
- [27] D.D. Yu, J. Bai, H.O. Liang, J.Z. Wang, C.P. Li, *Appl. Surf. Sci.* 349 (2015) 241–250.
- [28] J.X. Xia, M.X. Ji, J. Di, B. Wang, S. Yin, Q. Zhang, M.Q. He, H.M. Li, *Appl. Catal. B-Environ.* 191 (2016) 235–245.
- [29] M.X. Ji, J.X. Xia, J. Di, Y.L. Liu, R. Chen, Z.G. Chen, S. Yin, H.M. Li, *Chem. Eng. J.* 331 (2018) 355–363.
- [30] C.C. Han, L. Ge, C.F. Chen, Y.J. Li, Z. Zhao, X.L. Xiao, Z.L. Li, J.L. Zhang, *J. Mater. Chem. A* 2 (2014) 12594–12600.
- [31] J.L. Song, X. Wang, C.C. Wong, *Electrochim. Acta* 173 (2015) 834–838.
- [32] J. Di, J.X. Xia, Y.P. Ge, H.P. Li, H.Y. Ji, H. Xu, Q. Zhang, H.M. Li, M.N. Li, *Appl. Catal. B-Environ.* 168 (2015) 51–61.
- [33] G.J. Liu, J.Y. Shi, F.X. Zhang, Z. Chen, J.F. Han, C.M. Ding, S.S. Chen, Z.L. Wang, H.X. Han, C. Li, *Angew. Chemie Int. Ed.* 53 (2014) 7295–7299.
- [34] D.S. Dai, L. Wang, N. Xiao, S.S. Li, H. Xu, S. Liu, B.R. Xu, D. Lv, Y.Q. Gao, W.Y. Song, L. Ge, J. Liu, *Appl. Catal. B-Environ.* 233 (2018) 194–201.
- [35] X.Y. Wu, K.Q. Li, Y. Li, G.K. Zhang, *Nanoscale* 10 (2018) 15294–15302.
- [36] K. Fuku, R. Hayashi, S. Takakura, T. Kamegawa, K. Mori, H. Yamashita, *Angew. Chemie Int. Ed.* 52 (2013) 7446–7450.
- [37] H. Xu, S.S. Li, L. Ge, C.C. Han, Y.Q. Gao, D.S. Dai, *Int. J. Hydrogen Energy* 42 (2017) 22877–22886.
- [38] X.L. Jin, L.Q. Ye, H. Wang, Y.R. Su, H.Q. Xie, Z.G. Zhong, H. Zhang, *Appl. Catal. B-Environ.* 165 (2015) 668–675.
- [39] C. Hu, T.W. Peng, X.X. Hu, Y.L. Nie, X.F. Zhou, J.H. Qu, H. He, *J. Am. Chem. Soc.* 132 (2010) 857–862.
- [40] C. Liang, C.G. Niu, H. Guo, D.W. Huang, X.J. Wen, S.F. Yang, G.M. Zeng, *Catal. Sci. Technol.* 8 (2018) 1161–1175.